p-Type semiconducting nickel oxide as an efficiency-enhancing anode interfacial layer in polymer bulk-heterojunction solar cells

Michael D. Irwin, D. Bruce Buchholz, Alexander W. Hains, Robert P. H. Chang*, and Tobin J. Marks*

Department of Chemistry, Department of Materials Science and Engineering, and Materials Research Center, Northwestern University, 2145 Sheridan Road, Evanston, IL 60208

Contributed by Tobin J. Marks, December 21, 2007 (sent for review September 12, 2007)

To minimize interfacial power losses, thin (5–80 nm) layers of NiO, a *p*-type oxide semiconductor, are inserted between the active organic layer, poly(3-hexylthiophene) (P3HT) + [6,6]-phenyl-C_{61} butyric acid methyl ester (PCBM), and the ITO (tin-doped indium oxide) anode of bulk-heterojunction ITO/P3HT:PCBM/LiF/Al solar cells. The interfacial NiO layer is deposited by pulsed laser deposition directly onto cleaned ITO, and the active layer is subsequently deposited by spin-coating. Insertion of the NiO layer affords cell power conversion efficiencies as high as 5.2% and enhances the fill factor to 69% and the open-circuit voltage (V_{oc}) to 638 mV versus an ITO/P3HT:PCBM/LiF/Al control device. The value of such hole-transporting/electron-blocking interfacial layers is clearly demonstrated and should be applicable to other organic photovoltaics.

interface | photovoltaic | solar energy

In a world of ever-increasing energy demands and the need for renewable energy resources, photovoltaics are becoming an increasingly appealing option for energy production (1). Organic photovoltaic (OPV) cells (2–8) offer a potential alternative to conventional Si solar cells, as exemplified by (*i*) dye-sensitized (9), (*ii*) polymer (10), and (*iii*) small-molecule (11) cells. Of these, polymer cells offer the combined attraction of low cost, light weight, mechanical flexibility, and amenability to manufacture by high-throughput, low-cost, large-area reel-to-reel coating processes. It is estimated that such solar cells could be commercially viable if power conversion efficiencies (PCEs) on the order of ~10% were achieved (12). To date, the highest PCE polymer solar cells have been fabricated with an active layer composed of a blend of regioregular poly(3-hexylthiophene) (P3HT) (13) and the fullerene derivative [6,6]-phenyl-C_{61} butyric acid methyl ester (PCBM) (14) (Fig. 1). The P3HT + PCBM blend forms a phase-separated "bulk-heterojunction" (BHJ) nanostructure that provides a large interfacial area for exciton dissociation. When photo-excited, the P3HT network acts as an electron donor and transporter of holes to the cell anode, while the PCBM network acts as an electron acceptor and transporter of electrons to the cell cathode (10, 15–19). While one materials limitation of this BHJ design is doubtless the less than optimum match of the narrow P3HT:PCBM optical absorption to the solar spectrum (12), it is also likely that the multiple, poorly understood interfaces represent a significant and generic performance constraint to this type of solar cell.

Nanoscale "engineering" of the anode–organic interface has been successfully implemented in organic light-emitting diodes (OLEDs) for enhancing electrode–organic interfacial physical and electrical contact, resulting in reduced turn-on voltage, blocking of misdirected carriers, enhanced thermal durability, and increased current/power efficiency (20–24). In BHJ OPVs, interfacial effects probably limit realization of the maximum theoretical open-circuit voltage (V_{oc}). It is generally thought that the magnitude of V_{oc} parallels the energetic difference between the highest occupied molecular orbital (HOMO) of the BHJ donor material and the lowest unoccupied molecular orbital (LUMO) of the acceptor material (25–28). This difference, less the exciton binding energy, defines the theoretical maximum V_{oc}; however, in actual devices, the output is typically 300–500 mV less than this maximum. The hypothesized source of this loss is the field-driven nature of the devices, the presence of dark current, and Schottky barriers formed at the interfaces (28). One way to enhance OPV performance would then be to suppress these losses to the greatest extent possible. An effective electron-blocking layer (EBL)/hole-transporting layer (HTL) could, in principle, achieve this goal by preventing current leakage and consequent counterdiode formation (29).

In the simplest P3HT:PCBM BHJ cells, a blended solution of P3HT + PCBM in a 1:1 (wt:wt) ratio is typically spin-cast onto tin-doped indium oxide (ITO)-coated glass, which serves as the anode, and is annealed to form the active layer. The cell is then completed and its area defined by the sequential deposition of LiF and Al as the cathode (Fig. 1*A*). Note that inherent to the simplest BHJ cell architecture, the active layer donor and acceptor materials are both in direct contact with the anode, and it is possible for the acceptor material (PCBM) to transfer electrons to the hole-collecting anode, thereby compromising cell efficiency. P3HT:PCBM cells having this architecture typically exhibit PCEs of 2.7–2.9% where PCE is defined in Eq. **1**, with P_{out} the power output of the device, P_{in} the power of incident light source (mW/cm^2), and J_{sc} the short-circuit current density (mA/cm^2).

$$PCE = \frac{P_{out}}{P_{in}} = \frac{V_{oc}J_{sc}FF}{P_{in}} \quad [1]$$

To prevent electron leakage from the BHJ acceptor to the anode, to aid in photogenerated hole extraction, and to planarize the ITO surface, a thin semiconducting poly(3,4-ethylenedioxythiophene):poly(styrenesulfonate) (PEDOT:PSS) electron-blocking layer (EBL) is typically spin-cast as an aqueous dispersion onto the ITO before active layer deposition (Fig. 1*B*). This device design has achieved confirmed power efficiencies up to 4% (10). Despite these positive characteristics, note that aqueous PEDOT:PSS dispersions are at pH ~ 1 and corrosive to the ITO anode (30, 31). Furthermore, many researchers find that PEDOT:PSS depositions yield inconsistent film morphologies and electrical properties in accord with the demonstrated electrical inhomogeneity of these films (32, 33). Finally, polymer light-

Author contributions: M.D.I., R.P.H.C., and T.J.M. designed research; M.D.I., D.B.B., and A.W.H. performed research; M.D.I., D.B.B., A.W.H., R.P.H.C., and T.J.M. analyzed data; and M.D.I., D.B.B., A.W.H., R.P.H.C., and T.J.M. wrote the paper.

The authors declare no conflict of interest.

*To whom correspondence may be addressed. E-mail: r-chang@northwestern.edu or t-marks@northwestern.edu.

This article contains supporting information online at www.pnas.org/cgi/content/full/0711990105/DC1.

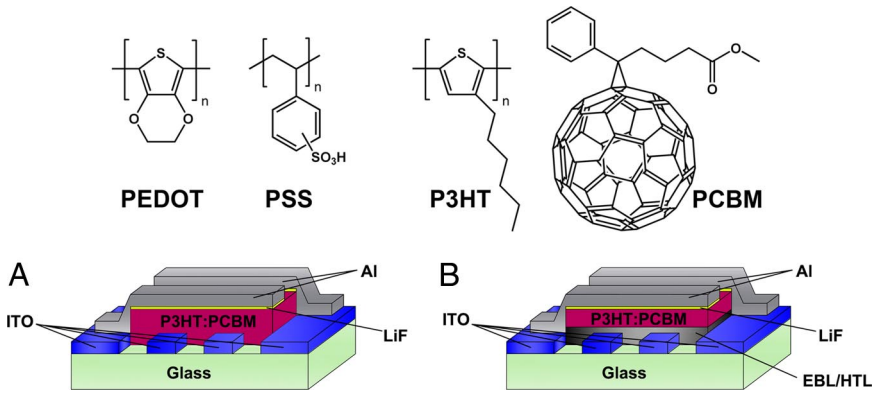

Fig. 1. Schematic drawings of the bulk-heterojunction photovoltaic device structures used here without (*A*) and with (*B*) an interfacial electron-blocking layer/hole-transporting layer (EBL/HTL). The chemical structures of PEDOT:PSS and the active layer components P3HT and PCBM are also shown.

emitting diode results show that PEDOT:PSS is an inefficient electron-blocking layer, reducing device current efficiency due to electron leakage to the anode (21, 22, 24, 30). This combination of limitations motivates replacement of PEDOT:PSS by a more suitable material for optimum OPV performance.

Realistic PEDOT:PSS replacements are subject to several fundamental constraints. (*i*) Sufficient optical transparency to allow solar photon access to the active layer, requiring wide band-gap semiconductors ($E_{gap} > 3$ eV) transparent in the visible spectral region. (*ii*) Effective blocking of electron leakage to the anode while efficiently transporting holes to the anode. This capability would address the aforementioned shortcoming of BHJ cells having both donor and acceptor active layer materials in direct contact with both electrodes. All other things being equal, a wide band-gap *p*-type semiconductor should be far more resistive to electron than to hole transport provided that the conduction band minimum (CBM) is sufficiently above the LUMO of the organic donor (and hence also the organic acceptor) material. (*iii*) Appropriate energy level alignment to allow ohmic contact to the donor material. (*iv*) Ambient chemical stability and inertness with respect to the adjacent device layers (34–36).

The device structure reported here incorporates NiO, a cubic wide band-gap semiconductor, which is essentially transparent as very thin layers and is *p*-type to facilitate hole conduction (i.e., acts as a HTL) (37–39). Previously, Yang *et al.* used *n*-type V_2O_5 (40, 41) and MoO_3 (42) as interfacial layers in BHJ OPVs; however, reported efficiencies less than those for optimized PEDOT:PSS-based devices (34). It will be seen here that NiO has a band structure well suited for P3HT:PCBM OPVs and provides an ohmic contact to P3HT while having a sufficiently high CBM to function as an EBL. Easily deposited NiO is shown here to be an effective PEDOT:PSS replacement and to afford both exceptional fill factor (*FF*) and open-circuit voltage (V_{oc}) metrics, as well as a BHJ cell power conversion efficiency of 5.2%.

Results and Discussion

To investigate the present OPV interlayer concept, a well studied model BHJ materials system was chosen, and the oxide *p*-type semiconductor was applied to the anode as a thin film (see *Materials and Methods* for details). The cell structure (see Fig. 1) employs P3HT as the donor and PCBM as the acceptor material, with the relevant energy levels shown in Fig. 2. As noted above, NiO was chosen as the *p*-type interfacial layer. Although arguably the most studied and modeled of binary transition metal oxides, exact details of the band structure, band-gap (E_g), Fermi level (E_f), conduction band minimum (CBM), valence band maximum (VBM), and conduction mechanism continue to stimulate discussion (39, 43–45). Near-stoichiometric NiO has a room temperature conductivity of $\approx 10^{-12}$ S/cm (45); however, Ni^{2+} vacancies are readily formed in undoped NiO that substantially increase the conductivity (39, 46), and films with conductivities of $\approx 10^{-3}$ to 10^{-4} S/cm have been reported (47). Additional discussion of the energy level orderings is presented below.

Thin films of *p*-NiO were deposited by pulsed laser deposition (PLD) on patterned ITO anodes, and the presence of crystalline NiO was confirmed by glancing-angle x-ray diffraction (GA-XRD) (Fig. 3). The characteristic NiO (111) and (200) reflections are clearly visible along with the ITO background (44). The morphology of the present NiO surfaces was surveyed by SEM and AFM [see supporting information (SI)]. The AFM and SEM images reveal distinct grains remarkably similar to those of the ITO

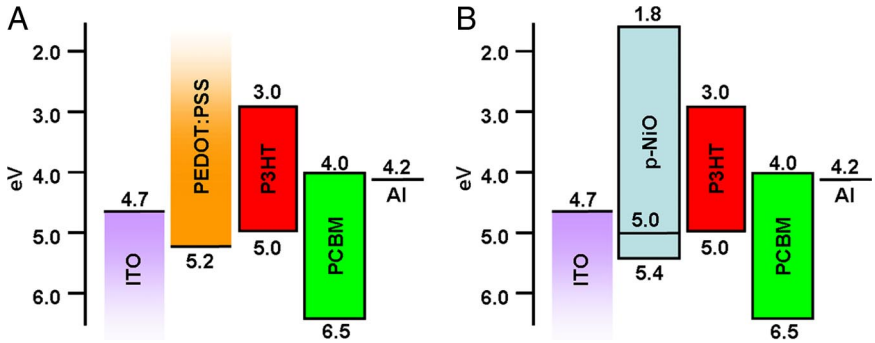

Fig. 2. Energy level diagrams of device components referenced to the vacuum level. (*A*) Typical P3HT:PCBM BHJ OPV with a PEDOT:PSS hole transport layer. (*B*) Device structure reported here. The published valence band, conduction band, and the Fermi level energies of NiO are shown.

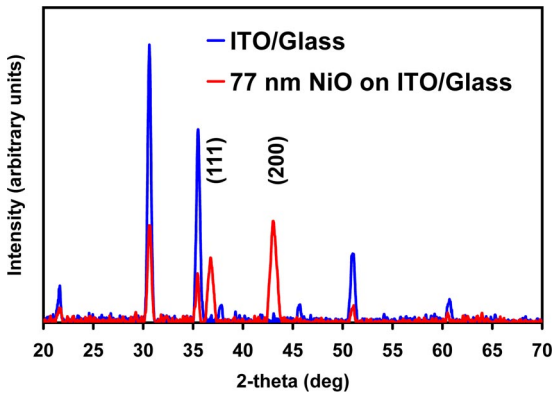

Fig. 3. Glancing-angle x-ray diffraction patterns of a NiO film grown on ITO/glass and the ITO/glass background. Features are labeled with the corresponding (*hkl*) reflections of cubic phase NiO.

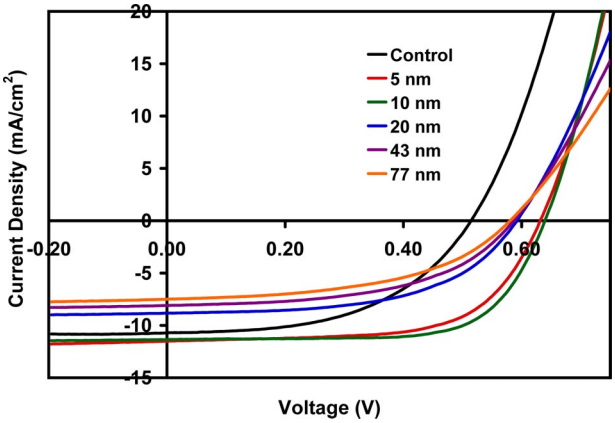

Fig. 5. Current density–voltage plots for glass/ITO/NiO/P3HT:PCBM/LiF/Al BHJ solar cells fabricated with varying layer thicknesses of NiO on the ITO anode. The control device has the structure: glass/ITO/P3HT:PCBM/LiF/Al.

surface, as expected. The NiO deposition process significantly planarizes the anode surface from an RMS roughness of 4–5 nm for bare glass/ITO to 1.0–1.5 nm for glass/ITO/NiO. PLD-derived NiO films on ITO are found to be highly transparent for 5- to 10-nm layers (Fig. 4) and should allow the maximum photon flux to reach the active layer for photo-current generation.

To prepare the active BHJ layer, an *o*-dichlorobenzene (ODCB) solution of P3HT and PCBM was spin-coated in a glove box onto the ITO/NiO surface. Within the glove box, the film was annealed and device fabrication was completed by vapor-depositing LiF and then the Al cathode. Preliminary optimization of the *p*-NiO interlayer for maximum OPV performance was carried out by varying the O_2 partial pressure during film growth, and the optimum O_2 partial pressure was found to be 7.0×10^{-4} Torr. The effect of NiO film thickness on device response was also investigated, and there is a clear trend of decreasing cell efficiency with increasing NiO thickness (Fig. 5). Series resistance and incident photon absorption by NiO are likely the dominant factors here (for dark *J–V* curves, see SI). The optimum NiO interlayer thickness was found to be 5–10 nm, where an 80% increase in PCE versus the control is observed. Additionally, inclusion of 10-nm NiO results in a slight increase (6%) in J_{sc} versus the control with a 24% increase in V_{oc} and a 37% increase in *FF*. External quantum efficiency (EQE) was measured on a device containing a 10-nm NiO layer and was found to reach a maximum of 87% between 400 and 700 nm (for EQE data, see SI). Response parameters for all NiO interlayer-based devices are summarized in Table 1 along with a community-standard device having the structure glass/ITO/PEDOT:PSS/-P3HT:PCBM/LiF/Al. The largest PCE measured was 5.2%.

An essential requirement for an effective OPV anode interfacial layer is that it provide a temporally durable device. At NiO interlayer thicknesses of 5 and 10 nm, a "break-in" period is observed (common in organic light-emitting diodes) where device response increases over the first few days after fabrication. It is hypothesized that these changes reflect active layer phase separation/reconstruction (10, 19) or polymer diffusion into the NiO grain boundaries, thus increasing the available surface area for charge collection. The performance of 10-nm-NiO devices reaches a maximum of ≈5.2% PCE and then slowly declines with continuous testing under AM1.5G radiation to ≈4.7%, where it remains essentially constant (Fig. 6). Although data are not shown, devices with a 5-nm NiO interlayer exhibit negligible temporal decay from a maximum PCE of ≈4.7% over the same time period. Devices containing a 20-nm or thicker NiO interlayer display flat device performance and no decay over time with continuous testing.

The reported optical band-gap of NiO ranges from 3.4 eV (47) to 4.3 eV (38) depending exactly on how the location of the band edge is defined: location of the first absorption feature, midpoint of the first rise, or where the maximum slope of absorption extrapolates to zero (38). In this contribution, the optical band-gap is determined from a standard plot of $(\alpha h\nu)^2$ versus $h\nu$, where α is the absorption coefficient and $h\nu$ is energy in eV; the x axis intercept of the linear portion of the plot is then taken as the optical band-gap. This yields a slightly lower value for the band-gap (3.6 eV) but as shown, even at the measured value, the band-gap is more than sufficient to serve as an effective electron-blocking layer (Fig. 2*B*). Note that some weak absorption in the

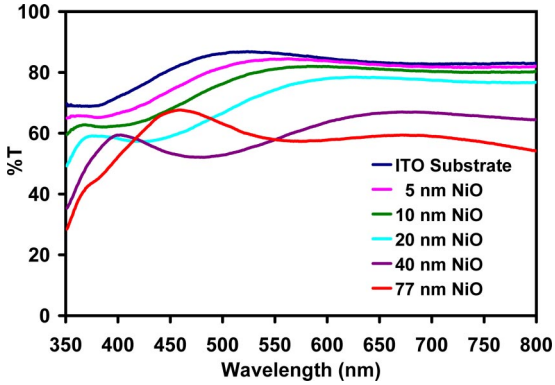

Fig. 4. Optical transmission spectra of various-thickness NiO films grown on ITO/glass. ITO/glass is included as the blank.

Table 1. Response parameters for the glass/ITO/interlayer/P3HT:PCBM/LiF/Al BHJ photovoltaic devices in Fig. 4

Device	V_{oc}, V	J_{sc}, mA/cm^2	*FF*, %	Efficiency, %
40-nm PEDOT:PSS	0.624	9.54	40.4	2.40
Control	0.515	10.7	50.7	2.87
5-nm NiO	0.634	11.5	63.3	4.75
10-nm NiO	0.638	11.3	69.3	5.16
20-nm NiO	0.591	8.83	55.2	2.96
43-nm NiO	0.586	8.09	52.4	2.55
77-nm NiO	0.581	7.49	49.8	2.23

The control has the structure: glass/ITO/P3HT:PCBM/LiF/Al. Interlayers in the device column are deposited directly onto ITO.

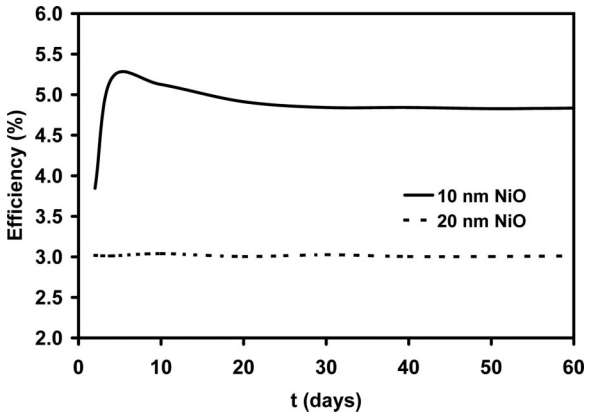

Fig. 6. Temporal response characteristics of two sets of BHJ devices with NiO anode layer thicknesses of 10 nm (solid line) and 20 nm (dashed line) on ITO.

visible range occurs due to low oscillator strength *d–d* interband transitions (37, 48); however, the overall transparencies of these thin NiO films are quite high (Fig. 4). The reported E_f for undoped NiO ranges from 3.8 eV (49) to 5.4 eV (50) and has been found to depend on the deposition substrate (51) and the NiO surface treatment (49). A frequently cited value is 5.0 eV (20, 23, 44, 52) while the valence band maximum (VBM) of undoped NiO is ~0.4 eV below E_f (Fig. 2*B*) (52, 53). In the present BHJ devices, NiO functions as both a hole-transport and an electron-blocking layer. Because of the essentially ohmic contact between NiO and P3HT (Fig. 2*B*), a large Schottky barrier is not formed, allowing holes to freely transfer from the active layer to the Ni^{2+} vacancy-based (excess O) hole-conducting anode band. The VBM of NiO is ~0.4 eV below the Fermi level ($E_f = 5.0$ eV), and with a NiO band-gap of ≈3.6 eV, the conduction band energy is ≈1.8 eV, while the LUMOs of P3HT and PCBM are at 3.0 and 4.0 eV, respectively. This energetic ordering should provide a 1.2- to 2.2-eV barrier to electron collection at the anode. These level energetics are important because the donor and acceptor materials are both in contact with the electrodes in BHJ cells, and it is energetically favorable for an electron from the PCBM LUMO to be collected at the anode [here, the ITO work function (Φ) is ≈4.7 eV]. This electron flow opposes the built-in field created by the differences in the anode and cathode work functions (Al, $\Phi = 4.2$ eV), and this, in turn, creates an opposing field and an overall decrease in positive cell potential (a decrease in V_{oc}).

The P3HT HOMO lies at 5.0 eV, while the PCBM LUMO lies at 4.0 eV. Thus, the theoretical V_{oc} maximum for this type of P3HT-PCBM BHJ cell is 1.0 V (energy levels were determined by thin-film solution cyclic voltammetry), but without any anode interfacial layer, the experimental V_{oc} is commonly near 0.50 V, representing a 500-mV loss. Importantly, the 10-nm NiO EBL recovers ~140 mV of the lost potential by increasing V_{oc} 40% from 0.515 V of the control device to 0.638 V. The effectiveness of the NiO EBL can doubtlessly be improved by further optimizing growth conditions because the present layer was found to be somewhat "leaky" in metal–insulator–semiconductor structures (see SI). This should further increase the V_{oc}.

Conclusions

The results of this study show that replacement of PEDOT:PSS with a *p*-type oxide semiconductor anode interfacial layer in an archetypical BHJ photovoltaic device results in a dramatic performance increase, while exhibiting excellent device stability. Inserting a 5- to 10-nm *p*-NiO layer in a P3HT:PCBM BHJ device increases the performance to 5.2% power conversion efficiency and should be extendable to other *p*-type materials of appropriate work function. These results also highlight the general importance of suppressing OPV interfacial losses, and their adverse effects on V_{oc} and power conversion efficiency.

Materials and Methods

Materials. PCBM was purchased from American Dye Source and was further purified by several cycles of sonication in toluene followed by filtration, and then sonication in pentane, followed by centrifugation. P3HT was purchased from Rieke Metals and was further purified by sequential Soxhlet extractions with methanol and hexanes.

Substrate Preparation. ITO-coated glass (10 Ω/□) was purchased from Delta Technologies in 25 × 75-mm strips. These were patterned to make two electrically separate 3-mm strips by applying a mask and dipping in hot concentrated HCl for 10 sec. The substrate was then quenched in saturated $NaHCO_3$ solution, dried, and sonicated in hexanes at 50°C for 30 min. The ITO was next cut into 25 × 12.5-mm substrates and cleaned by sonicating in 50°C aqueous detergent for 30 min, DI water for 5 min, and finally methanol, isopropanol, and acetone, respectively, for 30 min each. The solvent-cleaned substrates were further cleaned, immediately before use, in a UV-ozone cleaner for 10 min under ambient atmosphere.

NiO Film Growth. NiO films were grown by pulsed-laser deposition (PLD). A 248-nm KrF excimer laser with a 25-ns duration and a repetition rate of 2–5 Hz was used. The 230 mJ per pulse beam was focused onto a 1 × 2-mm spot on the NiO target. The target, ≈25 mm in diameter, was rotated at 5 rpm to prevent localized heating, and the laser pulses were swept cyclically across the target radius to additionally prevent localized heating. The target-substrate separation was fixed at 10 cm. An ambient O_2 atmosphere at a pressure between 2×10^{-2} and 2×10^{-5} torr was maintained during the NiO film deposition. The same system configuration was also used for the deposition of gold contacts from a metallic gold target: ≈13-mm-diameter target; 5 Hz; 135 mJ per pulse; deposition ambient 5×10^{-3} torr argon.

Patterned NiO films were fabricated either by shadow mask or by prepatterning the substrates with AZ-1518 photoresist and postdeposition lift-off. Films patterned by shadow mask were used in the fabrication of solar cells. Films patterned with AZ-1518 were used for step-edge film thickness measurements and fabrication of NiO/n-Si diode structures. Film thicknesses were measured with a Tencor P-10 profilometer. NiO film crystallinity was examined by glancing-angle ($\omega = 0.4°$) θ-2θ scan x-ray diffractometry on a computer-interfaced Rigaku ATX-G instrument using Ni-filtered Cu Kα radiation. Current–voltage characterization of NiO/n-Si diode structures was performed with a Keithley 237 source meter. Optical transparency was measured with a Varian Cary 1E spectrophotometer in dual-beam transmission (T) mode. A Hitachi S4800 instrument was used for SEM imaging, and a ThermoMicroscopes CP Research instrument was used for AFM imaging in the tapping mode.

BHJ OPV Device Fabrication. A solution of P3HT (20 mg) and PCBM (20 mg) was prepared in purified *o*-dichlorobenzene (1.0 ml, distilled from P_2O_5) the day before fabrication. The solution was stirred overnight in the dark at 50°C under nitrogen and was then sonicated at 50°C for 1 h the next day. The active layer solution and the cleaned substrates were immediately transferred to a nitrogen-filled glove box (<1 ppm O_2 and H_2O), and the active layer solution was spin-coated onto bare ITO or the ITO/NiO anodes at 550 rpm for 60 sec, then 2,000 rpm for 1 sec (thickness = 210–230 nm). Contact areas were cleaned with dry toluene and a cotton swab, and the films were then annealed on a hot plate in the glove box at 120°C for 10 min. In the glove box, LiF/Al (0.6 nm/130 nm) cathodes were next deposited sequentially without breaking vacuum, using a thermal evaporator. The rates used were 0.1 Å/sec for LiF (Acros; 99.98%) and ≈2 Å/sec for Al (Sigma–Aldrich; 99.999%), with a chamber pressure of 1.1×10^{-6} torr. The cathodes were deposited through a shadow mask with two 2.0-mm strips perpendicular to the two patterned ITO strips to make four devices per substrate. Finally, the completed solar cells were encapsulated with a glass slide by using UV-curable epoxy (Electro-Lite ELC-2500), which was cured in a UV chamber inside of the glove box.

BHJ OPV *I–V* Characterization. Device evaluation was performed at 298 K by using a Class A Spectra-Nova Technologies solar cell analyzer having a xenon lamp that simulates AM1.5G light from 400 to 1,100 nm. The instrument was calibrated with a monocrystalline Si diode fitted with a KG3 filter to bring spectral mismatch to unity. The calibration standard was calibrated by the National Renewable Energy Laboratory (NREL). Four-point contacts were

made to the substrate with Ag paste and copper alligator clips (28, 54). Individual devices were isolated by a mask during testing to avoid current collection from adjacent devices and edge effects. A device fabricated and tested on the above instrument having the structure glass/ITO/PEDOT:PSS/-P3HT:PCBM/LiF/Al exhibited a J_{sc} = 9.5 mA/cm^2, in agreement with the literature (10). Devices containing a 20-nm NiO interlayer where tested at the NREL, and the results mirrored those obtained at Northwestern University.

ACKNOWLEDGMENTS. We thank B. Leever, A. Martinson, and M. McCain for assistance with data collection; Prof. J. Hupp for generous access to his EQE instrumentation; and K. Emery and T. Moriarty of the NREL for device characterization and very helpful discussions. This work was supported by BP Solar and Department of Energy Grant DE-FG02–06ER46320. The characterization facilities are supported by the National Science Foundation–Materials Research Science and Engineering Centers program through the Northwestern University Materials Research Center (Grant DMR-0520513).

1. Morton O (2006) Solar energy: A new day dawning? Silicon Valley sunrise. *Nature* 443:19–22.
2. Lira-Cantu M, Krebs FC (2005) Polymer photovoltaics: From conjugated polymers to hybrid organic-inorganic solar cells. *Rec Res Devel Appl Phys* 8:71–98.
3. Dennler G, Lungenschmied C, Neugebauer H, Sariciftci NS, Labouret A (2005) Flexible, conjugated, polymer-fullerene-based bulk-heterojunction solar cells: Basics, encapsulation, and integration. *J Mater Res* 20:3224–3233.
4. Gledhill SE, Scott B, Gregg BA (2005) Organic and nano-structured composite photovoltaics: An overview. *J Mater Res* 20:3167–3179.
5. Coakley KM, Liu Y, Goh C, McGehee MD (2005) Ordered organic-inorganic bulk heterojunction photovoltaic cells. *MRS Bull* 30:37–40.
6. Grätzel M (2005) Dye-sensitized solid-state heterojunction solar cells. *MRS Bull* 30:23–27.
7. Shaheen SE, Ginley DS, Jabbour GE (2005) Organic-based photovoltaics. Toward low-cost power generation. *MRS Bull* 30:10–19.
8. Günes S, Neugebauer H, Sariciftci NS (2007) Conjugated polymer-based organic solar cells. *Chem Rev* 107:1324–1338.
9. Kuang D, *et al.* (2007) High-efficiency and stable mesoscopic dye-sensitized solar cells based on a high molar extinction coefficient ruthenium sensitizer and nonvolatile electrolyte. *Adv Mater (Weinheim, Germany)* 19:1133–1137.
10. Li G, *et al.* (2005) High-efficiency solution processable polymer photovoltaic cells by self-organization of polymer blends. *Nat Mater* 4:864–868.
11. Mutolo KL, *et al.* (2006) Enhanced open-circuit voltage in subphthalocyanine/C_{60} organic photovoltaic cells. *J Am Chem Soc* 128:8108–8109.
12. Scharber MC, *et al.* (2006) Design rules for donors in bulk-heterojunction solar cells—towards 10% energy-conversion efficiency. *Adv Mater (Weinheim, Germany)* 18:789–794.
13. Chen TA, Rieke RD (1992) The first regioregular head-to-tail poly(3-hexylthiophene-2,5-diyl) and a regiorandom isopolymer: Nickel versus palladium catalysis of 2(5)-bromo-5(2)-(bromozincio)-3-hexylthiophene polymerization. *J Am Chem Soc* 114:10087–10088.
14. Hummelen JC, *et al.* (1995) Preparation and characterization of fulleroid and methanofullerene derivatives. *J Org Chem* 60:532–538.
15. Inoue K, *et al.* (2005) High efficiency P3HT/PCBM solar cell. *Mater Res Soc Symp Proc* 836:69–74.
16. Kim K, Liu J, Namboothiry MAG, Carroll DL (2007) Roles of donor and acceptor nanodomains in 6% efficient thermally annealed polymer photovoltaics. *Appl Phys Lett* 90:163511.
17. Li G, Shrotriya V, Yao Y, Yang Y (2005) Investigation of annealing effects and film thickness dependence of polymer solar cells based on poly(3-hexylthiophene). *J Appl Phys* 98:043704.
18. Reyes-Reyes M, Kim K, Carroll DL (2005) High-efficiency photovoltaic devices based on annealed poly(3-hexylthiphene) and 1-(3-methoxycarbonyl)-propyl-1-phenyl-(6,6)C61 blends. *Appl Phys Lett* 87:083506.
19. Yang X, *et al.* (2005) Nanoscale morphology of high-performance polymer solar cells. *Nano Lett* 5:579–583.
20. Chan IM, Hsu T-Y, Hong FC (2002) Enhanced hole injections in organic light-emitting devices by depositing nickel oxide on indium tin oxide anode. *Appl Phys Lett* 81:1899–1901.
21. Huang Q, Evmenenko G, Dutta P, Marks TJ (2003) Moleculary ''engineered'' anode adsorbates for probing OLED interfacial structure-charge injection/luminance relationships: Large, structure-dependent effects. *J Am Chem Soc* 125:14704–14705.
22. Huang Q, *et al.* (2005) Covalently bound hole-injecting nanostructures. Systematics of molecular architecture, thickness, saturation, and electron-blocking characteristics on organic light-emitting diode luminance, turn-on voltage, and quantum efficiency. *J Am Chem Soc* 127:10227–10242.
23. Im HC, *et al.* (2007) Highly efficient organic light-emitting diodes fabricated using nickel-oxide buffer layers between the anodes and the hole transport layers. *Thin Solid Films* 515:5099–5102.
24. Yan H, *et al.* (2005) High-performance hole-transport layers for polymer light-emitting diodes. Implementation of organosiloxane cross-linking chemistry in polymeric electroluminescent devices. *J Am Chem Soc* 127:3172–3183.
25. Derouiche H, Djara V (2007) Impact of the energy difference in LUMO and HOMO of the bulk heterojunctions components on the efficiency of organic solar cells. *Sol Energy Mater Sol Cells* 91:1163–1167.
26. Forrest SR (2006) Organic photovoltaic cells: Strategies for increasing solar energy conversion efficiencies. *Polym Mater Sci Eng* 95:160.
27. Koster LJA, Mihailetchi VD, de Boer B, Blom PWM (2006) Modeling of poly(3-hexylthiophene):methanofullerene bulk-heterojunction solar cells. *Proc SPIE Int Soc Opt Eng* 6192:61920A.
28. Moliton A, Nunzi J-M (2006) How to model the behaviour of photovoltaic cells. *Polym Int* 55:583–600.
29. Hains AW, Martinson ABF, Irwin MD, Yan H, Marks TJ (2007) Bulk-heterojunction organic solar cells: Interfacial engineering routes to increased open-circuit voltage and power conversion efficiency. *Polym Mater Sci Eng* 96:814–815.
30. Kim Y-H, Lee S-H, Noh J, Han S-H (2006) Performance and stability of electroluminescent device with self-assembled layers of poly(3,4-ethylenedioxythiophene)–poly(styrenesulfonate) and polyelectrolytes. *Thin Solid Films* 510:305–310.
31. Ni J, *et al.* (2005) MOCVD-derived highly transparent, conductive zinc- and tin-doped indium oxide thin films: Precursor synthesis, metastable phase film growth and characterization, and application as anodes in polymer light-emitting diodes. *J Am Chem Soc* 127:5613–5624.
32. Kemerink M, Timpanaro S, De Kok MM, Meulenkamp EA, Touwslager FJ (2004) Three-dimensional inhomogeneities in PEDOT:PSS films. *J Phys Chem B* 108:18820–18825.
33. Ionescu-Zanetti C, Mechler A, Carter SA, Lal R (2004) Semiconductive polymer blends: Correlating structure with transport properties at the nanoscale. *Adv Mater (Weinheim, Germany)* 16:385–389.
34. Shrotriya V, Li G, Yao Y, Chu C-W, Yang Y (2006) Transition metal oxides as the buffer layer for polymer photovoltaic cells. *Appl Phys Lett* 88:073508.
35. Takahashi K, *et al.* (2007) Efficiency increase by insertion of electrodeposited CuSCN into ITO/organic solid interface in bulk hetero-junction solar cells consisting of polythiophene and fullerene. *Chem Lett* 36:762–763.
36. White MS, Olson DC, Shaheen SE, Kopidakis N, Ginley DS (2006) Inverted bulk-heterojunction organic photovoltaic device using a solution-derived ZnO underlayer. *Appl Phys Lett* 89:143517.
37. Fujimori A, Minami F (1984) Valence band photoemission and optical absorption in nickel compounds. *Phys Rev B* 30:957–971.
38. Hüfner S (1994) Electronic structure of NiO and related 3d-transition-metal-compounds. *Adv Phys* 43:183–356.
39. Pizzini S, Morlotti R (1967) Thermodynamic and transport properties of stoichiometric and nonstoichiometric nickel oxide. *J Electrochem Soc* 114:1179–1189.
40. Gledel C, Audiere JP, Clement R (1989) Elaboration and characterization of amorphous V_2O_5 thin films-silicon p-n junctions. *J Mater Sci* 24:2493–2496.
41. Hardee KL, Bard AJ (1977) Semiconductor Electrodes: X. Photoelectrochemical behaviour of several polycrystalline metal oxide electrodes in aqueous solutions. *J Electrochem Soc* 124:215–224.
42. Werfel F, Minni E (1983) Photoemission study of the electronic structure of Mo and Mo oxides. *J Phys C Solid State Phys* 16:6091–6100.
43. Adler D, Feinleib J (1970) Electrical and optical properties of narrow-bands materials. *Phys Rev B* 2:3112–3134.
44. Schmahl NG, Barthel J, Eikerling GF (1964) Röntgenographische Untersuchungen an den Systemen MgO–CuO und NiO–CuO. *Z Anorg Allg Chem* 332:230–237.
45. Wittenauer MA, Van Zandt LL (1982) Surface conduction versus bulk conduction in pure stoichiometric NiO crystals. *Philos Mag B* 46:659–667.
46. Lany S, Osorio-Guillen J, Zunger A (2007) Origin of the doping asymmetry in oxides: Hole doping in NiO versus electron doping in ZnO. *Phys Rev B* 75:241203.
47. Patil PS, Kadam LD (2002) Preparation and characterization of spray pyrolyzed nickel oxide (NiO) thin films. *Appl Surf Sci* 199:211–221.
48. Ohta H, Kamiya M, Kamiya T, Hirano M, Hosono H (2003) UV-detector based on pn-heterojunction diode composed of transparent oxide semiconductors, p-NiO/n-ZnO. *Thin Solid Films* 445:317–321.
49. McKay JM, Henrich VE (1985) Surface electronic structure of NiO: Defect states, O_2 and H_2O interactions. *Phys Rev B* 32:6764–6772.
50. Madjid AH, Martinez JM (1972) Thermionic emission from nickel oxide. *Phys Rev Lett* 28:1313–1315.
51. Nakasa A, Adachi M, Usami H, Suzuki E, Taniguchi Y (2006) Fabrication of nickel oxide and Ni-doped indium tin oxide thin films using pyrosol process. *Thin Solid Films* 498:240–243.
52. Nakaoka K, Ueyama J, Ogura K (2004) Semiconductor and electrochromic properties of electrochemically deposited nickel oxide films. *J Electroanal Chem* 571:93–99.
53. Hüfner S, *et al.* (1991) The electronic structure of NiO investigated by photoemission spectroscopy. *Solid State Commun* 80:869–873.
54. Shrotriya V, *et al.* (2006) Accurate measurement and characterization of organic solar cells. *Adv Funct Mater* 16:2016–2023.